

Alternating Repetition Time Balanced Steady State Free Precession

J. Leupold,^{1*} J. Hennig,¹ and K. Scheffler²

A novel balanced SSFP technique for the separation or suppression of different resonance frequencies (e.g., fat suppression) is presented. The method is based on applying two alternating and different repetition times, TR_1 and TR_2 . This RF scheme manipulates the sensitivity of balanced SSFP to off-resonance effects by a modification of the frequency response profile. Starting from a general approach, an optimally broadened stopband within the frequency response function is designed. This is achieved with a TR_2 being one third of TR_1 and an RF-pulse phase increment of 90° . With this approach TR_2 is too short (~ 1 ms) to switch imaging gradients and is only used to change the frequency sensitivity. Without a significant change of the spectral position of the stopband, TR_1 can be varied over a range of values (~ 2.5 – 4.5 ms) while TR_2 and phase cycling is kept constant. On-resonance spins show a magnetization behavior similar to balanced SSFP, but with maximal magnetization at flip angles about 10° lower than in balanced SSFP. The total scan time is increased by about 30% compared to conventional balanced SSFP. The new technique was applied on phantoms and volunteers to produce rapid, fat suppressed images. Magn Reson Med 55:557–565, 2006. © 2006 Wiley-Liss, Inc.

Key words: Balanced SSFP; steady state; frequency response function; spectral separation; fat suppression

Balanced SSFP (TrueFISP, FIESTA, b-FFE, bSSFP) shows high SNR at short repetition times (1,2) and is frequently used in applications that require high temporal resolution, such as in cardiac imaging or perfusion studies. The T_2/T_1 -weighted contrast of bSSFP generates a bright fat signal ($T_2/T_1 \sim 0.3$) comparable to the signal intensity of liquids or fluids. A separation or suppression of fat signals is thus essential for, e.g., coronary artery imaging (3) or cartilage imaging (4), or in general, to separate different resonances or metabolites.

Several methods have been proposed to generate frequency selective bSSFP images. A simple and robust approach is FS-SSFP (spectral or fat saturated SSFP) (5), where magnetization is longitudinally stored after an $\alpha/2$ flipback pulse, thereby offering an interruption of the steady state and making the insertion of a spectral selective saturation pulse possible. A different method is FEMR (fluctuating equilibrium MR) (6), which is based on a mod-

ification of the frequency response function of bSSFP generated by modified phase cycling schemes. Two resonances, such as fat and water images, can be acquired simultaneously in an interleaved manner. In LC-SSFP (linear combination SSFP) (7,8), several images with different frequency responses are combined to generate a shaped frequency sensitivity. A similar approach is based on binominal excitation patterns (9) or on the direct synthesis of shaped frequency response function (10). A further possibility is to use the phase difference of the fat and water spins for separation, either by direct phase detection (11) or Dixon-type post processing (12–15).

An intrinsic drawback of FEMR, LC-SSFP, binominal excitation patterns (9), and similar variants (16) is the large increase ($\sim 100\%$) in total acquisition time to generate the required frequency response function, as well as a restriction of possible repetition times TR . FS-SSFP shows an increase in total imaging time of about 30%, depending on the number of steady state interruptions during which a spectral selective saturation pulse is played out, and is not restricted in TR . FS-SSFP is regarded to be the most robust fat suppressing SSFP method (4,5); however, only a single resonance can be detected.

The method introduced here is based on the new concept of using two different and apparently independent repetition times, TR_1 and TR_2 , and a tailored RF phase cycling (17). The specific sequence parameters, such as TR_2/TR_1 ratio and phase cycling scheme, are derived from a general approach designed to produce a shaped steady state frequency response profile with broad stop- and passband. The cyclic variation of repetition times offers a further mechanism not only to shape, but also a new parameter to control the periodicity of the frequency response profile.

THEORY

The conventional bSSFP sequence consists of a train of RF-pulses with flip angle α equidistantly spaced by TR . The phase of the RF-pulse is incremented by 180° from pulse to pulse. Imaging gradients are applied on the x-, y-, and z-axis with vanishing zeroth moment within one repetition period. In the steady state, the magnetization vector immediately after RF excitation consists of the three components $M_x = M_0(E_1 - 1)E_2 \sin \alpha \sin \theta / D$, $M_y = M_0(1 - E_1) \sin \alpha (1 + E_2 \cos \theta) / D$, and $M_z = M_0(1 - E_1)[E_2(E_2 + \cos \theta) + (1 + E_2 \cos \theta) \cos \alpha] / D$, with $E_1 = \exp(-TR/T_1)$, $E_2 = \exp(-TR/T_2)$, and $D = (1 - E_1 \cos \alpha)(1 + E_2 \cos \theta) - E_2(E_1 - \cos \alpha)(E_2 + \cos \theta)$ (from (18), including RF phase increment of 180°). θ is the dephasing during TR due to chemical shift or local B_0 field variations. For $TR \ll T_2$, the signal for on-resonance spins ($\theta = 0^\circ$) is maximized at $\alpha = \arccos[(T_1/T_2 - 1)/(T_1/T_2 + 1)]$ (19), and the resulting signal magnitude is proportional to $(T_2/T_1)^{1/2}$.

¹Department of Diagnostic Radiology, Medical Physics, University Hospital Freiburg, Freiburg, Germany. ²MR Physics, Department of Medical Radiology, University Hospital of Basel, Basel, Switzerland.

Grant Sponsor: German Research Foundation DFG; Grant Number: SP632/2–1. Grant Sponsor: Swiss National Science Foundation; Grant Number: PP00B-68783.

*Correspondence to: Jochen Leupold, University Hospital Freiburg, Department of Diagnostic Radiology, Medical Physics, Hugstetter Strasse 55, 79106 Freiburg, Germany. E-mail: jochen.leupold@uniklinik-freiburg.de

Received 10 June 2005; revised 4 October 2005; accepted 27 October 2005. DOI 10.1002/mrm.20790

Published online 30 January 2006 in Wiley InterScience (www.interscience.wiley.com).

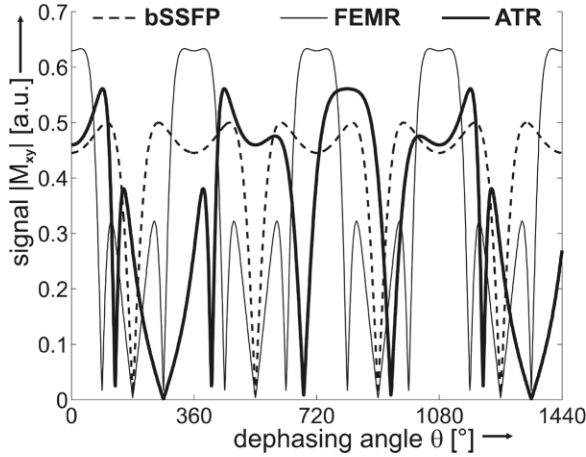


FIG. 1. Simulated frequency response functions of bSSFP (dashed line), FEMR (narrow solid line), and ATR (bold solid line, plotted is FS-ATR with $\tau = TR_2/TR_1 = 1/3$ and RF pulse phase cycle 0° 90° 180° 270°). Simulations have been performed with $T_1 = T_2 = 300$ ms. Repetition times and flip angles: bSSFP: $TR = 3.46$ ms, $\alpha = 63^\circ$; FEMR: $TR = 3.46$ ms, $\alpha = 50^\circ$; ATR: $TR_1 = 3.46$ ms, $TR_2 = 1.15$ ms, $\alpha = 50^\circ$. FEMR shows a stopband at $\theta_{\text{stop}} = 180^\circ$; ATR shows a stopband at $\theta_{\text{stop}} = 270^\circ$.

The dependency of the magnitude of the transversal magnetization component on θ (Fig. 1, dashed line) is $1/TR$ -periodic and shows up experimentally as the banding artifact. According to this frequency response function (FRF), an isochromat with $\theta = 180^\circ$ or odd integer multiples thereof is largely suppressed and appears dark in the image. In practice, this stopband is too narrow to give a robust spectral selection or suppression technique.

Balanced SSFP with Alternating TR

A novel approach to broaden the stopband of the FRF is based on alternating TR (ATR) and modified RF-pulse phases (Fig. 2) (17). In general, alternating repetition times TR_1 and TR_2 ($TR_1 \geq TR_2$) with $\tau = TR_2/TR_1$ produces an FRF that is no longer 2π periodic as in bSSFP, but has a periodicity of $2\pi/\tau$ (if $1/\tau$ is an integer value), for which an integer multiple of 2π dephasing occurs both within TR_1 and TR_2 . The resulting ATR steady state signal can be calculated as follows: without loss of generality, the phase ϕ_1 of the first RF-pulse can be set to zero, as a constant phase added to each RF-pulse does not change the magnitude of the FRF, and $TR_2 \leq TR_1$. The steady state magnetization after pulse RF_1 is

$$\vec{M}_1^+ = \mathbf{R}_1 \mathbf{D}_2 \vec{M}_2^+ + \mathbf{R}_1 M_0 (1 - E_{12}) \vec{z} \quad [1]$$

and equivalently after pulse RF_2

$$\vec{M}_2^+ = \mathbf{R}_2 \mathbf{D}_1 \vec{M}_1^+ + \mathbf{R}_2 M_0 (1 - E_{11}) \vec{z} \quad [2]$$

Combination of Eq. [1] and Eq. [2] yields the steady state magnetization

$$\vec{M}_1^+ = (1 - \mathbf{R}_1 \mathbf{D}_2 \mathbf{R}_2 \mathbf{D}_1)^{-1} [\mathbf{R}_1 \mathbf{D}_2 \mathbf{R}_2 M_0 (1 - E_{11}) \vec{z} + \mathbf{R}_1 M_0 (1 - E_{12}) \vec{z}] \quad [3]$$

with the matrix \mathbf{D}_1 representing relaxation and dephasing by θ during TR_1 , with $E_{21} = \exp(-TR_1/T_2)$, and $E_{11} = \exp(-TR_1/T_1)$

$$\mathbf{D}_1 = \begin{bmatrix} E_{21} \cos \theta & E_{21} \sin \theta & 0 \\ -E_{21} \sin \theta & E_{21} \cos \theta & 0 \\ 0 & 0 & E_{11} \cos \theta \end{bmatrix} \quad [4]$$

and matrix \mathbf{D}_2 representing relaxation and dephasing $\tau\theta$ during TR_2 , with $\tau = TR_2/TR_1 \leq 1$, $E_{22} = \exp(-TR_2/T_2)$, and $E_{12} = \exp(-TR_2/T_1)$.

$$\mathbf{D}_2 = \begin{bmatrix} E_{22} \cos(\tau\theta) & E_{22} \sin(\tau\theta) & 0 \\ -E_{22} \sin(\tau\theta) & E_{22} \cos(\tau\theta) & 0 \\ 0 & 0 & E_{12} \cos(\theta\tau) \end{bmatrix} \quad [5]$$

The RF-pulse matrices $\mathbf{R}_{1,2}$ include the influence of RF excitation (exemplarily shown for $\alpha = 90^\circ$ and arbitrary phase ϕ_2 of second RF-pulse):

$$\mathbf{R}_1 = \begin{bmatrix} 1 & 0 & 0 \\ 0 & 0 & 1 \\ 0 & -1 & 0 \end{bmatrix} \quad [6]$$

$$\mathbf{R}_2 = \begin{bmatrix} \cos^2 \phi_2 & \frac{1}{2} \sin(2\phi_2) & -\sin \phi_2 \\ \frac{1}{2} \sin(2\phi_2) & \sin^2 \phi_2 & \cos \phi_2 \\ \sin \phi_2 & -\cos \phi_2 & 0 \end{bmatrix} \quad [7]$$

With these rotation and relaxation matrices, the steady state after RF_1 of the sequence can be computed. A similar calculation starting with Eq. [1] and Eq. [2] gives the steady state \vec{M}_2^+ after RF_2 in dependence of \mathbf{R}_1 , \mathbf{R}_2 , \mathbf{D}_1 , \mathbf{D}_2 , M_0 , E_{11} , and E_{12} . As will be shown later, TR_2 is in general too short to switch imaging gradients after RF_2 ; only the steady state after RF_1 is analyzed. In that case, TR_1 takes over the role

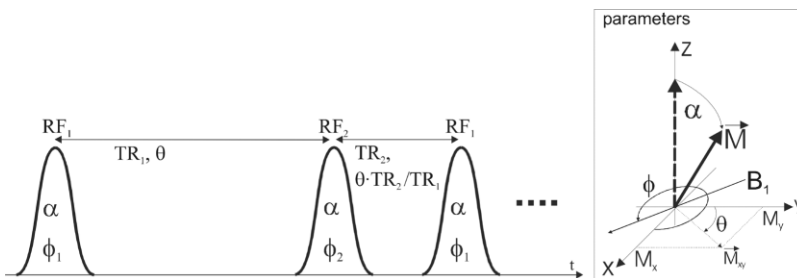


FIG. 2. Left: Generic alternating TR sequence (ATR) with constant flip angle α and two excitation pulses RF_1 and RF_2 with arbitrary phases ϕ_1 and ϕ_2 . An isochromat with accumulated dephasing angle θ during TR_1 experiences a dephasing of $\theta \cdot TR_2/TR_1$ during TR_2 . Right: depiction of parameters used in Eqs. [1]–[7].

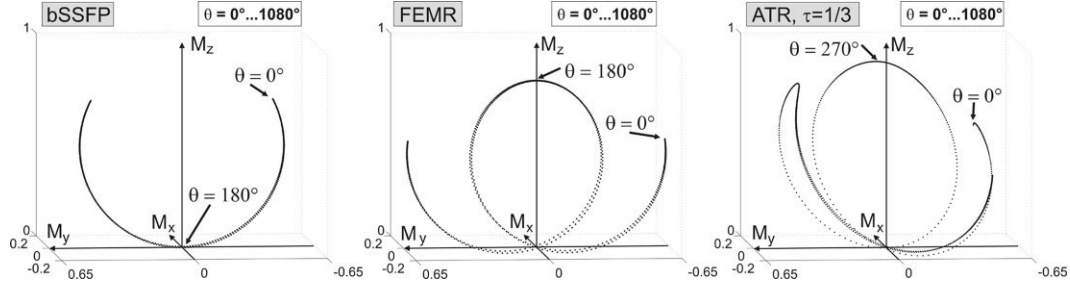


FIG. 3. Simulated 3D distribution of magnetization for $0^\circ \leq \theta \leq 1080^\circ$ at echo time $TR/2$ for bSSFP, FEMR, and ATR (FS-ATR with $\tau = TR_2/TR_1 = 1/3$ and RF pulse phase cycle $0^\circ 90^\circ 180^\circ 270^\circ$, signal at echo time $TR_1/2$). Note the high density of longitudinal states at $\theta = 180^\circ$ (FEMR) and at $\theta = 270^\circ$ (FS-ATR), which leads to a broad stopband. Parameters for simulation are identical to parameters in Fig. 1.

of TR in bSSFP, while RF_2 and TR_2 are only means to change the shape of the FRF.

ATR gives a dual steady state and can introduce a new mechanism for generating stopbands. In conventional bSSFP, the stopband emerges because of a nearly completely saturated spin-system at certain off-resonance angles. For alternating TR, however, one steady state configuration is composed mainly of longitudinal magnetization (producing a transverse stopband); the other steady state configuration is a mixture of longitudinal and transverse magnetization (passband), as depicted in Fig. 3, where the 3D location of the steady state magnetization, i.e., the tip of the magnetization vector, of bSSFP, FEMR, and ATR is plotted for a range of off-resonance angles θ from 0° to 1080° (corresponding to the periodicity of the simulated ATR sequence).

RF Phase Cycling for Balanced SSFP with Alternating TR

In the following, conditions for the free parameters $\tau = TR_1/TR_2$ and phase ϕ_2 of the second RF-pulse RF_2 will be deduced to produce a broad stopband generated by longitudinal magnetization at a certain dephasing θ_{stop} . If longitudinal magnetization $\vec{M}_1 = (0 \ 0 \ 1)$ is one possible steady state solution, \vec{M}_1 is an eigenvector of the composite matrix $\mathbf{R}_1 \mathbf{D}_2 \mathbf{R}_2 \mathbf{D}_1$ (neglecting relaxation, $E_{11} = E_{12} = E_{21} = E_{22} = 1$) with eigenvalue 1. Solving $\mathbf{R}_1 \mathbf{D}_2 \mathbf{R}_2 \mathbf{D}_1 \vec{M}_1 = \vec{M}_1$ leads to the condition

$$\phi_2 - \tau \theta_{\text{stop}} = -180^\circ \quad [8]$$

which connects the position of the stopband, θ_{stop} , with the phase ϕ_2 of RF_2 . To make the stopband robust against local field inhomogeneities, it should be as broad as possible with a symmetric shape around θ_{stop} . This symmetry condition in combination with Eq. [3] leads to the second constraint for ϕ_2 given by

$$\phi_2 = -180^\circ/(\tau + 1) \quad [9]$$

Combining Eqs. [8] and [9] finally gives

$$\theta_{\text{stop}} = -\phi_2 \quad [10]$$

for the location of the stopband. Then, due to symmetry, there is a passband with its center located at $\theta_{\text{pass}} = -\theta_{\text{stop}} = \phi_2$ (the pulse phase ϕ_2 is always negative, see Eq. [9]).

The resulting steady state of the transversal magnetization M_{xy} is shown in Fig. 4 for a range of $1/25 \leq \tau \leq 1$. For ATR, the position of the stop- and passbands depends on τ (see Eqs. [9] and [10]). Therefore, in order to position the passband at on-resonance frequency, the entire FRF has to be shifted accordingly, which means the passbands shall be at $\theta_{\text{pass}} = 0$ and no longer at $\theta_{\text{pass}} = \phi_2$. This results in a shift of the FRF by $\delta\theta = -\theta_{\text{pass}} = \theta_{\text{stop}} = -\phi_2$ and places the stopband finally at $\theta_{\text{stop}} = -2\phi_2 = 360^\circ/(\tau + 1)$. This shift of the FRF can be produced by adding a phase cycle with alternating increment ϕ_{inc} , which is for the two RF-pulses RF_1 and RF_2 given by

$$\phi_{\text{inc}} = \begin{cases} -\delta\theta & \text{for } RF_2 \\ -\delta\theta \cdot \tau & \text{for } RF_1 \end{cases} \quad [11]$$

The ATR frequency responses depicted in Fig. 4 are calculated using the conditions given in Eqs. [9] and [10], and

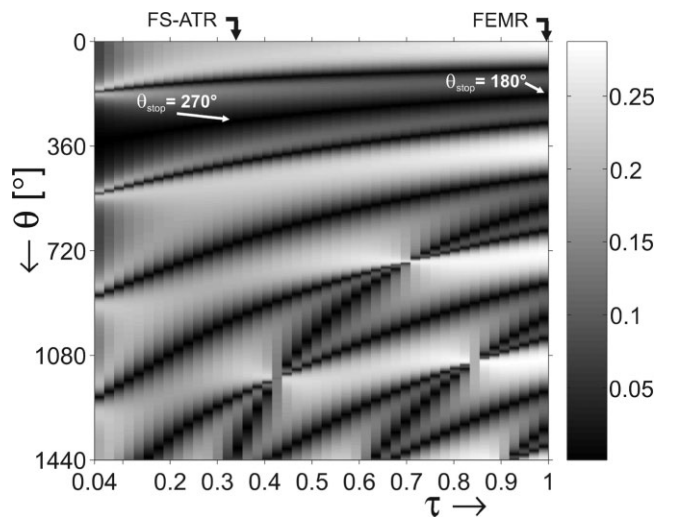


FIG. 4. Transversal component of FRF of ATR with $1/25 \leq \tau \leq 1$ (FS-ATR: $\tau = 1/3$, FEMR: $\tau = 1$). RF-pulse phases are adjusted to obtain symmetric minimum and shift of the maximum to $\theta = 0^\circ$. Simulation parameters are $T_1 = 500$ ms, $T_2 = 100$ ms, $\alpha = 50^\circ$, variation of τ carried out with $TR_1 = 3.46$ ms and $TR_2 = \tau \cdot TR_1$.

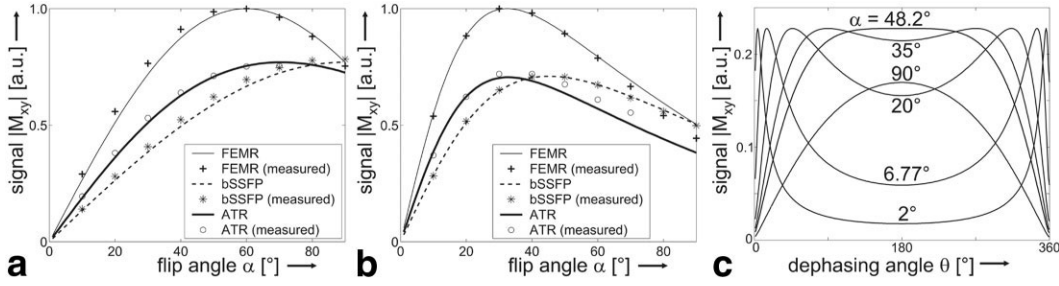


FIG. 5. Simulated and measured flip angle dependency of on-resonance signal amplitude for bSSFP, FEMR, and FS-ATR with (a) $T_1 = T_2 = 300$ ms and (b) $T_1 = 520$ ms, $T_2 = 90$ ms. The signal maximum of FS-ATR appears at lower flip angles as for bSSFP. (c) Flip angle dependency of bSSFP-FRF to explain optimal flip angle of FS-ATR; see text.

with a shift of the passband to $\theta = 0^\circ$ using Eq. [11] as described.

Examples of different sequences and their appropriate parameter setting that can be derived from the general ATR concept are:

1. Conventional bSSFP with $TR_2 = TR_1 = TR$ and $\phi_2 = 180^\circ$.
2. FEMR (6) with $TR_2 = TR_1 = TR$ and $\phi_2 = 90^\circ$. Shift of the passband according to Eq. [11] gives 0° 180° 180° 0° phase cycle, and $\theta_{\text{stop}} = 180^\circ$. This method is designed to acquire water and fat images simultaneously in a k -space-interleaved manner. As the FRF alternates between even and odd sequence cycles, each phase encoding gradient is played out twice and assigned to the water or fat k -space. FEMR requires a certain TR to ensure $\theta = 180^\circ$ for fat spins during TR, i.e., $TR = 2.3$ ms or $TR = 6.9$ ms with a chemical shift of $\Delta f = 217$ Hz at 1.5T.
3. Wideband SSFP (20), which consists of alternated TR with phase cycle of 0° 180° 0° 180° , and aims to broaden the passband.

Balanced SSFP with Alternated TR Applied to Fat Suppression (FS-ATR)

Based on the described concept of ATR, a variant FS-ATR (fat suppressing ATR) can be designed with the following parameters and features: choosing $TR_1 = 3TR_2$, i.e., $\tau = 1/3$, it follows from Eq. [9] that $\phi_2 = -135^\circ$ ($\phi_1 = 0^\circ$), and from Eq. [10] $\theta_{\text{stop}} = 135^\circ$. To center the passband at $\theta = 0^\circ$, the FRF is shifted by 135° along the θ -axis using $\phi_{\text{inc}} = -135^\circ$ for pulse RF_2 and $\phi_{\text{inc}} = -45^\circ$ for pulse RF_1 , respectively, according to Eq. [11]. This leads to an RF phase cycle over all RF-pulses of 0° (pulse RF_1) – 270° (pulse RF_2) – 180° (pulse RF_1) – 450° (pulse RF_2) – 360° (pulse RF_1), which is equivalent to a 0° 90° 180° 270° 0° cycle, i.e., a constant phase increment for each RF-pulse regardless of the difference in TR_1 and TR_2 . Then, the stopband minimum is located at $\theta_{\text{stop}} = 270^\circ$, which is practicable as it requires $TR_1 = 3.46$ and $TR_2 = 3.46/3$ ms = 1.15 ms for fat to dephase by 270° during TR_1 . In principle, also, shorter τ values than $1/3$ are possible, resulting in a slightly increased stopband broadness. However, for fat suppression at 1.5 T the restriction

$$TR_1 + TR_2 = 1/\Delta f = 4.3 \text{ ms} \quad [12]$$

must be fulfilled. Eq. [12] is derived by combining $\theta_{\text{fat}} = TR_1 \cdot \Delta f \cdot 360^\circ$ (the off-resonance angle that fat acquires during TR_1) and $\theta_{\text{stop}} = 360^\circ/(\tau + 1)$ (the stopband minimum of an FRF shifted in order to place a maximum on $\theta = 0^\circ$). The latter is the result of combining Eqs. [9] and [10] and carrying out a shift according to Eq. [11]. Then, setting $\theta_{\text{fat}} = \theta_{\text{stop}}$ will lead to Eq. [12].

Therefore, smaller τ can only be reached with a shorter TR_2 , which requires shorter RF-pulses as the length of the slice selection gradient (including ramps) determines the shortest possible TR_2 . Thus, shorter τ deteriorates the slice profile or increases SAR.

The fat-suppression ability of FS-ATR is visualized in Figs. 1 and 3, in comparison to conventional bSSFP and FEMR. For bSSFP, the minima or stopbands of the FRF are created by saturation; both the longitudinal and transverse part of the steady state magnetization is nearly zero at a stopband. As described in detail by Freeman and Hill (18), the density of steady states within a certain dephasing interval $\Delta\theta$ is not constant but varies with θ . It exhibits a small density around $\theta = 180^\circ$ (giving a narrow stopband) and high density around $\theta = 0^\circ$ (broad passband), as indicated by the density of the dots in Fig. 3. For FEMR and ATR, the density of steady states and thus the broadness of stop- and passbands as a function of dephasing θ is totally different. A high density of states composed of large longitudinal but almost vanishing transverse components is located for FS-ATR around $\theta = 270^\circ$ (FEMR: $\theta = 180^\circ$), which generates the broad stopband. RF_2 partially transfers this distribution into transverse magnetization to produce a broad passband before it is again transferred back into the longitudinal configuration by the next RF excitation RF_1 . If TR_2 is sufficiently long to switch imaging gradients, two different steady states can be recorded as in FEMR, one during TR_1 and one during TR_2 , i.e., the steady state alternates between two configurations. If TR_2 is short as in FS-ATR, only the FRF during TR_1 can be observed.

Optimal Flip Angle for FS-ATR

A practical issue is the increased power deposition of FS-ATR per unit time in comparison to bSSFP. Therefore, the maximal reachable flip angle within the SAR limit is lower. However, FS-ATR has maximal signal amplitude at flip angles lower than α_{opt} (bSSFP), as demonstrated in Fig. 5. This can be explained by the fact that for on-resonance

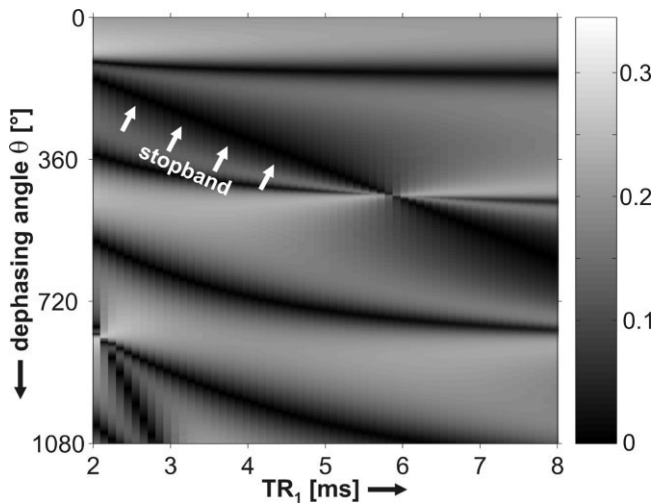


FIG. 6. Steady state FRF of FS-ATR as a function of TR_1 , with a constant TR_2 of 1.15 ms, $T_1 = 500$ ms, $T_2 = 100$ ms, and $\alpha = 50^\circ$. Note the linear relation of the stopband minimum with TR_1 , giving a robust fat suppression for different TR_1 within the range of 2.5 ms to 4.5 ms.

spins, FS-ATR becomes identical to bSSFP with an RF phase increment of 90° , if the small difference in relaxation during TR_1 and TR_2 is neglected. This RF phase increment shifts the FRF of bSSFP by -90° . In order to keep the maximum of the FRF at $\theta = 0^\circ$ the excitation angle has to be lowered accordingly, as the maximum amplitude of the FRF for bSSFP is constant for varying α within the limit $\alpha < \alpha_{opt}$, but is located at different positions on the θ -axis (18,21); see Fig. 5c.

TR_1 Insensitivity of FS-ATR

Eq. [8] offers the possibility to reach a stopband in ATR under variation of $TR_1 \rightarrow TR_1'$ while keeping TR_2 and RF-pulse phases constant. According to Eq. [8], the minimum moves to $\theta_{stop} = (180^\circ + \phi_2)/\tau'$, with $\tau' = TR_2/TR_1'$, and thus linearly depends on TR_1' . As a result, the fat resonance stays within the stopband even if TR_1 is changed. However, the symmetry condition Eq. [9] is broken, which slightly decreases the broadness of the stopband. The effect of varying TR_1 on the FRF of FS-ATR is demonstrated in Fig. 6. FS-ATR can be regarded to be largely TR_1 insensitive, as long as the stopband does not coincide with the narrow gaps at $\theta = 135^\circ$ and

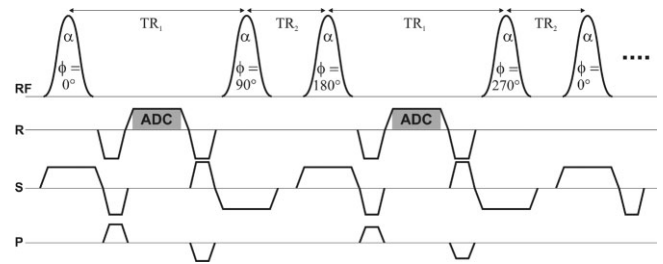


FIG. 8. Sequence diagram of FS-ATR with $\tau = 1/3$. The polarity of the slice selection gradient is alternated between excitations, and signal encoding and acquisitions is performed only during TR_1 . RF-pulse phase cycle has a constant increment of 90° .

$\theta = 405^\circ$ (see Figs. 1 and 6), i.e., for the range of about $2.5 \text{ ms} < TR_1 < 4.5 \text{ ms}$.

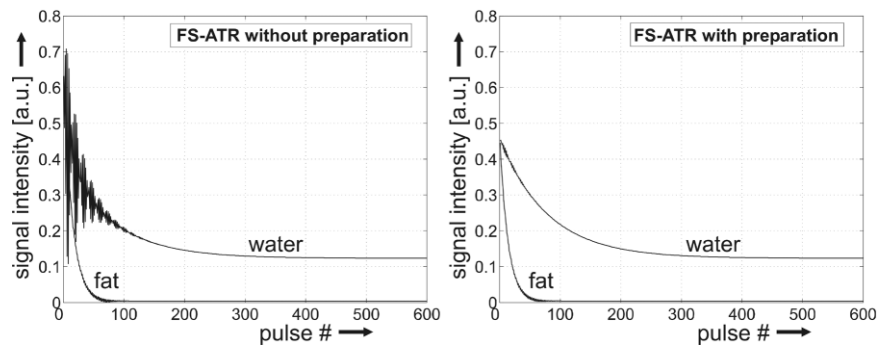
Initial FS-ATR Preparation

ATR shows signal oscillations during the transition into the steady state, which can lead to image artifacts. In analogy to the bSSFP - $\alpha/2$ preparation (22), the on-resonance magnetization vector can be aligned to its steady state position before the sequence starts. The preparation pulse for FS-ATR is played out at time $t_{prep} = TR_2$ before the first TR_1 interval. To determine the flip angle and phase of the preparation pulse, the steady state after the RF-pulse RF_2 with phase of 270° was simulated and the vector representing on-resonance spins was determined. The alignment of this vector and the alignment of the magnetization for on-resonance spins after the preparation pulse must be equal. The simulation gives a flip angle of $2\alpha/3$ and a phase of 225° for the preparation pulse. The signal evolution of FS-ATR with and without a preparation pulse is plotted in Fig. 7. For water spins (with relaxation times of blood), which are on-resonance, there are severe signal oscillations in the simulation at the beginning of the sequence without preparation. These oscillations are removed by the preparation pulse. Some slight oscillations remain; however, they are not expected to have significant influence on image quality.

IMPLEMENTATION AND EXPERIMENTS

The diagram of the implemented FS-ATR sequence is shown in Fig. 8. Due to the very short TR_2 of 1.15 ms and RF-pulse duration of about 600 to 1000 μs , the polarity of

FIG. 7. Simulated FS-ATR signal evolution into steady state for blood (on-resonance, $T_1 = 1.2$ s, $T_2 = 0.1$ s) and fat (270° off-resonance, $T_1 = 0.25$ s, $T_2 = 0.06$ s), $\alpha = 40^\circ$. Left: without initial preparation; right: with initial preparation pulse with flip angle of $2\alpha/3$ and pulse phase of 225° . Plotted signal values were calculated at echo time $TR_1/2$.



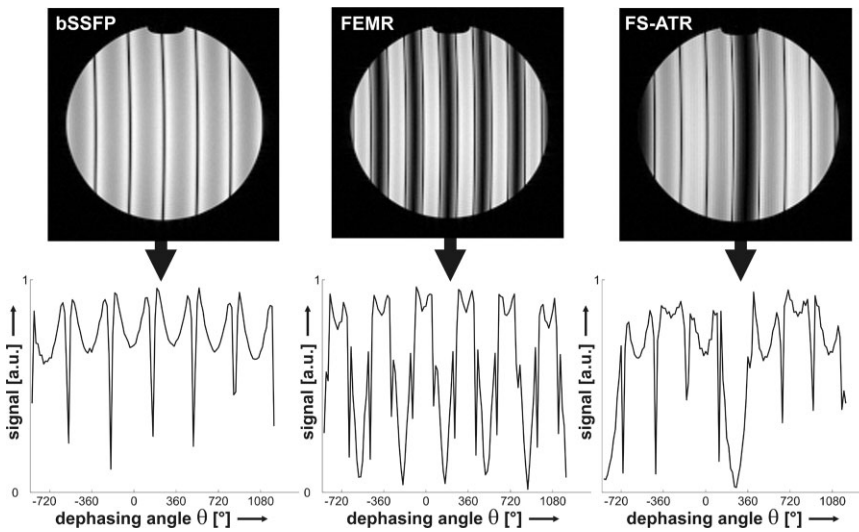


FIG. 9. Measured frequency responses of bSSFP, FEMR, and FS-ATR. Parameters according to simulation in Fig. 1. A shim gradient of 0.34 mT/m was applied in the readout direction (left-right) to create a range of off-resonance frequencies.

the slice selection gradient is alternated from RF-pulse to RF-pulse in order to save time during TR_2 . Otherwise, unipolar slice selection gradients would require additional rephasing and dephasing gradient lobes as in conventional bSSFP, which will need too much time to be switchable during a short TR_2 of 1.15 ms.

Experiments to evaluate signal intensities, frequency response profiles, and image quality of bSSFP, FEMR, and FS-ATR were performed on phantoms and healthy volunteers on a 1.5 T scanner (Sonata, Siemens Medical Solutions, Erlangen, Germany). All phantom experiments were performed with a receiving CP head coil. For the in vivo experiments, a CP spine array coil was used for receiving in combination with a CP body array coil for the abdominal images; knee images were performed with a CP flexible coil.

The FRF of bSSFP, FEMR, and FS-ATR were measured (Fig. 9) in a 2D acquisition with voxel size of $0.9 \text{ mm} \times 0.9 \text{ mm} \times 10 \text{ mm}$ on a bottle phantom ($T_1 = T_2 = 300 \text{ ms}$). A shim gradient of 0.34 mT/m was applied along the readout direction to create a range of off-resonance frequencies (17° per voxel). Parameters are corresponding to the simulations shown in Fig. 1: bSSFP: $TR = 3.47 \text{ ms}$, $\alpha = 63^\circ$; FEMR: $TR = 3.47 \text{ ms}$, $\alpha = 49^\circ$; FS-ATR: $TR_1 = 3.47 \text{ ms}$, $TR_2 = 1.15 \text{ ms}$, $\alpha = 50^\circ$.

Signal intensity versus excitation flip angle (Fig. 5) was experimentally verified for two different phantoms by evaluating an ROI in the fifth slice out of a 12-slices 3D image set. The relaxation times of the phantom used for Fig. 5a was $T_1 = T_2 = 300 \text{ ms}$. A second phantom with T_1

$= 520 \text{ ms}$ and $T_2 = 90 \text{ ms}$ was examined to show the flip angle dependency of the signal with a T_2/T_1 ratio smaller than one (Fig. 5b). Practically, relaxation times of fluid/blood are of interest, but in this case flow effects have to be considered to assess the flip angle dependency of the signal in vivo.

The fat suppression performance of FS-ATR and FEMR was compared on phantoms and volunteers. Figure 10a shows an image of two bottles (diameter 12 cm) of Gd-doped water ($T_1 = T_2 = 300 \text{ ms}$) with a small bottle (diameter 7.5 cm) with vegetable oil on top acquired with conventional bSSFP. Depicted are 2D acquisitions with 256×256 matrix size and in-plane resolution of $1.2 \text{ mm} \times 1.2 \text{ mm}$ and $\alpha = 60^\circ$. Fig. 10b has been acquired with FS-ATR using $TR_1 = 3.47 \text{ ms}$ and $TR_2 = 1.15 \text{ ms}$, and Fig. 10c with FEMR and $TR = 6.58 \text{ ms}$. The average signal of two ROIs (water and fat) was evaluated for each experiment. Abdominal 3D breath-hold images (Figs. 11–13) have been acquired with bSSFP, FEMR, and ATR using comparable acquisition parameters as for the phantom experiments. To demonstrate TR_1 insensitivity of FS-ATR, 3D high resolution images (Fig. 14, $0.8 \text{ mm} \times 0.8 \text{ mm}$) of the knee have been measured with the shortest possible but increased TR_1 of 4.29 ms ($TR_2 = 1.14 \text{ ms}$).

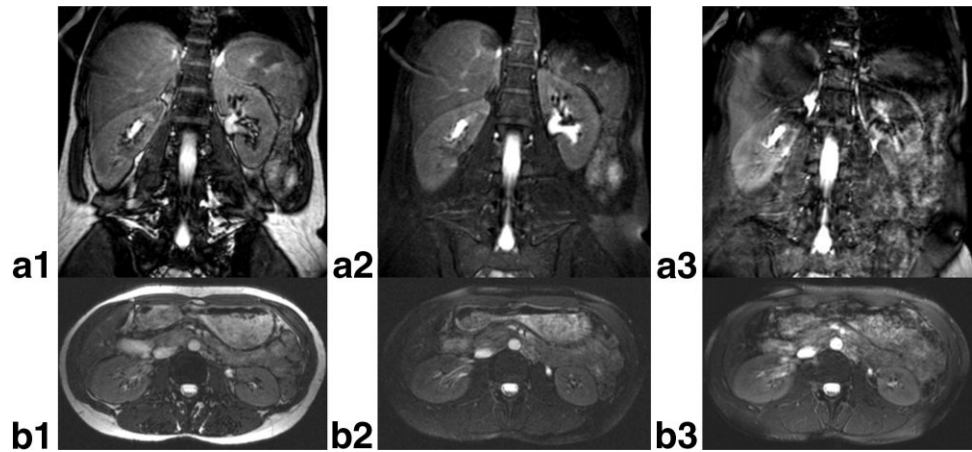
RESULTS

Figure 9 shows a clearly broadened stopband for ATR in comparison to FEMR and bSSFP. The overall signal max-



FIG. 10. 2D phantom experiments of two big water bottles with small fat bottle on top, $\alpha = 60^\circ$. Numbers are average signal values over ROIs in water and fat. (a) bSSFP, $TR = 3.47 \text{ ms}$. (b) FS-ATR, $TR_1 = 3.47 \text{ ms}$, $TR_2 = 1.15 \text{ ms}$. (c) FEMR, $TR = 6.58 \text{ ms}$. All images show identical windowing.

FIG. 11. Volunteer #1, abdominal images. Depicted slice with thickness 6 mm taken out of a 3D data set. Coronal images show in plane resolution of $1.4 \text{ mm} \times 2 \text{ mm}$; transversal images $1.2 \text{ mm} \times 1.7 \text{ mm}$, $\alpha = 40^\circ$. (a1) bSSFP ($TR = 3.46 \text{ ms}$), (b1) bSSFP ($TR = 3.64 \text{ ms}$), (a2) FS-ATR ($TR_1 = 3.046 \text{ ms}$, $TR_2 = 1.15 \text{ ms}$), (b2) FS-ATR ($TR_1 = 3.047 \text{ ms}$, $TR_2 = 1.15 \text{ ms}$), (a3) FEMR ($TR = 6.6 \text{ ms}$), (b3) FEMR ($TR = 6.58 \text{ ms}$). All images show identical windowing and identical slice position (except for possible differences in breath hold position).



imum of FS-ATR is not at $\theta = 0^\circ$ but at $\theta = 810^\circ$ for the given set of T_1 , T_2 , and α . Therefore, the images shown in Fig. 9 correspond well with the simulations in Fig. 1.

Phantom fat-water images presented in Fig. 10 show a similar fat suppression for ATR and FEMR. In both cases a sufficient field homogeneity within the phantom could be achieved to produce sharp resonances of both fat and water that are located precisely within the stop- and pass-band, respectively. According to the simulations and measurements shown in Fig. 5, FEMR gives a higher signal for both fat and water for an excitation flip angle of 60° . However, the signal ratio of water/fat is higher for FS-ATR. Experiments show the optimal flip angle for FS-ATR being smaller than the optimal flip angle for balanced SSFP (Fig. 5, $\alpha = 80^\circ$ and $\alpha = 90^\circ$; could not be measured for FS-ATR due to SAR limitations).

The in vivo fat suppression ability of FS-ATR and FEMR is demonstrated in Fig. 11 on volunteer #1 in coronal and transversal images. FS-ATR shows improved fat suppression compared to FEMR, and several artifacts are visible in the coronal FEMR image. In general, the fat suppression works better for the intraabdominal fat tissue; the suppression of the subcutaneous (s.c.) fat is not homogenous, most probably due to frequency variations induced by the imperfect shim. The homogeneity of fat suppression in FS-ATR is demonstrated in Fig. 12 on volunteer #2, where a maximum intensity projection through a transversal 3D block is shown. The same behavior is demonstrated in the coronal abdominal images of volunteer #3 in Fig. 13. In Fig. 14, the robustness of FS-ATR against variations of TR_1 is demonstrated; TR_1 was increased from 3.46 ms to

4.29 ms, while keeping RF-pulse phase cycling constant and TR_2 at 1.15 ms. Depicted is a slice with thickness of 3 mm, taken out of a 3D data set.

DISCUSSION

The method of alternating TR introduces a novel and general mechanism for the modification of the FRF of bSSFP-type sequences. By appropriate adjustment of the RF-pulse phases, at certain off-resonance frequencies the magnetization oscillates between longitudinal orientation and orientation with transverse part resulting in a broad stop- and passband. Signal is acquired during the long TR_1 (3.46 ms) whereas the short TR_2 (1.15 ms) is only used to modify the FRF. With this setup a broader stopband compared to FEMR can be achieved, which makes ATR less sensitive to field inhomogeneities. The maximal signal at the passband of ATR is identical to conventional bSSFP, but is achieved at a reduced flip angle compared to the optimal flip angle of bSSFP.

For FS-ATR with $\tau = 1/3$, the frequency separation Δf of the stop- and passband can be controlled within a certain range by changing TR_1 and TR_2 on condition that $TR_1 + TR_2 = 1/\Delta f$ (Eq. [12]), with RF phase cycle remaining unchanged. In general, any frequency separation Δf can be achieved with the appropriate choice of τ and corresponding RF phase cycling, as given by Eqs. [8]–[11]. This makes ATR also promising for chemical shift imaging of metabolites of nuclei different from protons (23). An important advantage of FS-ATR over other methods is its insensitivity to variations in TR_1 within a certain range given in Fig. 6. This can be used either to speed up acquisition by

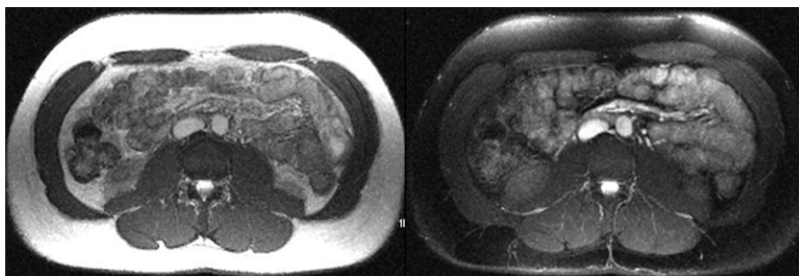


FIG. 12. Volunteer #2, abdominal images. Maximum intensity projection over 8 partitions with 2 mm thickness each, flip angle $\alpha = 40^\circ$, in-plane resolution $1.5 \text{ mm} \times 1.5 \text{ mm}$. Left: bSSFP ($TR = 3.4 \text{ ms}$); Right: FS-ATR ($TR_1 = 3.4 \text{ ms}$, $TR_2 = 1.2 \text{ ms}$).



FIG. 13. Volunteer #3, abdominal images. Depicted is the central slice with thickness of 4 mm of a 3D data set. Flip angle $\alpha = 35^\circ$, in-plane resolution $1.6 \text{ mm} \times 1.6 \text{ mm}$. Left: bSSFP ($\text{TR} = 3.3 \text{ ms}$); Right: FS-ATR ($\text{TR}_1 = 3.3 \text{ ms}$, $\text{TR}_2 = 1.14 \text{ ms}$).

lowering TR_1 , or to take account for the need of stronger gradients when increasing resolution by lengthening TR.

The scan time of FS-ATR is about 33% longer than for bSSFP, resulting in a loss of scan efficiency (SNR divided by total scan time). FEMR requires a longer and fixed TR of 6.6 ms to 6.8 ms (depending on the fat-water separation) and acquires each k -space line twice to produce both water and fat images. The increased TR of FEMR in combination with its higher steady state amplitude gives an increased scan efficiency compared to FS-ATR. However, if only a single resonance is of interest, FEMR is less efficient compared to FS-ATR. Especially in applications that require short total acquisition time, e.g., scans during breath hold (3), total scan time becomes more important than scan efficiency, as long as SNR is sufficiently high. However, in cases where both the water and fat image is of interest, FEMR or the binominal approach of Hardy and Dixon (9) would be the method of choice. FS-bSSFP requires a scan time comparable to FS-ATR, depending on the number of steady state interruptions (5). The general drawback of FS-bSSFP and other non-steady state techniques (24) is the sensitivity to off-resonance effects in terms of signal oscillations generated after each steady state interruption that can lead to artifacts. In contrast, FS-ATR and FEMR are continuous steady state techniques that show no artifacts due to signal oscillations.

The direct applicability of FS-ATR at 3 T is problematic since Eq. [12] requires very short repetition times of $\text{TR}_1 + \text{TR}_2 = 1/\Delta f(3T) = 2.3 \text{ ms}$. However, the FRF of ATR consists of three passbands (Fig. 1), allowing for a shift of

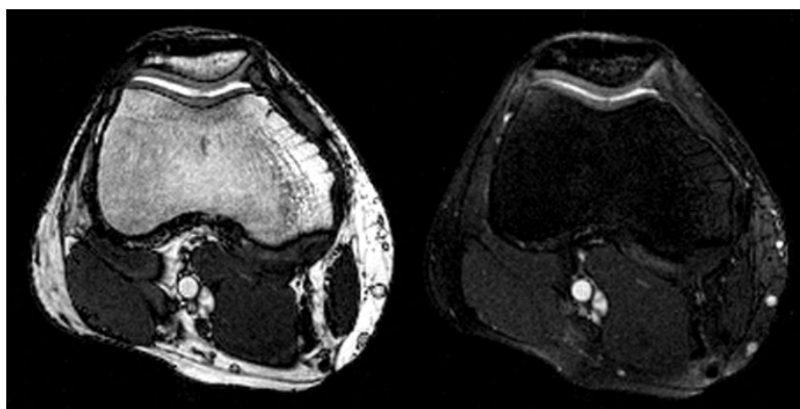
on-resonance spins to the second passband located at $\theta = 810^\circ$. With this trick, possible parameters for FS-ATR at 3T become $\text{TR}_1 = 3.46 \text{ ms}$, $\text{TR}_2 = 1.15 \text{ ms}$, and RF phase cycle $0^\circ 180^\circ 180^\circ 0^\circ$. This version produces an FRF with high on-resonance signal and stopband at $\theta = 540^\circ$, which is equal to the off-resonance angle of fat ($\Delta f = 434 \text{ Hz}$) at 3.46 ms at 3T.

The limiting factor of FS-ATR is the sensitivity to local field variations, which will dislocate the fat off-resonance frequency in the FRF and lead to visible fat (or vice versa, invisible water). However, these problems occur in any fat-suppressed bSSFP method. Due to the alternating polarity of the slice gradient, the first moment is not zero at the time of RF excitation. This might increase flow sensitivity; however, no severe flow artifacts have been observed for the abdominal acquisitions performed in this study.

CONCLUSION

We have presented a novel and easy to implement method to achieve fat suppressed bSSFP images. FS-ATR relies on the intrinsic behavior of off-resonance spins; it can tolerate shim variations over a practically useful range and does not require a certain repetition time, which makes it easy to change image parameters, e.g., increasing resolution. Total scan time is increased about 30% in comparison with bSSFP; thus, the method is promising for fast imaging during breath hold.

FIG. 14. Volunteer #4, knee images. Depicted is slice No. 6 with thickness of 3 mm of a 16 partitions 3D data set, with in-plane resolution of $0.8 \text{ mm} \times 0.8 \text{ mm}$. Left: bSSFP ($\text{TR} = 4.29 \text{ ms}$, $\alpha = 50^\circ$); Right: FS-ATR with $\text{TR}_1 = 4.29 \text{ ms}$ and $\text{TR}_2 = 1.15 \text{ ms}$. Note the time TR_1 , which was increased in comparison with Fig. 11.



REFERENCES

1. Carr HY. Steady state free precession in nuclear magnetic resonance. *Phys Rev* 1958;112:1693–1701.
2. Oppelt A, Graumann R, Barfuss H, Fischer H, Hartl W, Shajor W. FISP—a new fast MRI sequence. *Electromedica* 1986;54:15–18.
3. Deshpande VS, Shea SM, Laub G, Simonetti OP, Finn JP, Li D. 3D magnetization-prepared true-FISP: a new technique for imaging coronary arteries. *Magn Reson Med* 2001;46:494–502.
4. Hargreaves BA, Gold GE, Beaulieu CF, Vasanaawala SS, Nishimura DG, Pauly JM. Comparison of new sequences for high-resolution cartilage imaging. *Magn Reson Med* 2003;49:700–709.
5. Scheffler K, Heid O, Hennig J. Magnetization preparation during the steady state: fat-saturated 3D TrueFISP. *Magn Reson Med* 2001;45:1075–1080.
6. Vasanaawala SS, Pauly JM, Nishimura DG. Fluctuating equilibrium MRI. *Magn Reson Med* 1999;42:876–883.
7. Vasanaawala SS, Pauly JM, Nishimura DG. Linear combination steady state free precession MRI. *Magn Reson Med* 2000;43:82–90.
8. Bangerter NK, Hargreaves BA, Vasanaawala SS, Pauly JM, Gold GE, Nishimura DG. Analysis of multiple-acquisition SSFP. *Magn Reson Med* 2004;51:1038–1047.
9. Hardy C, Dixon W. Steady state free precession imaging with inherent fat suppression. In: *Proceedings of the 10th Annual meeting of ISMRM*, Honolulu, Hawaii, USA, 2002. p. 473.
10. Overall WR, Nishimura DG, Hu BS. Steady-state sequence synthesis and its application to efficient fat-suppressed imaging. *Magn Reson Med* 2003;50:550–559.
11. Hargreaves BA, Vasanaawala SS, Nayak KS, Hu BS, Nishimura DG. Fat-suppressed steady-state free precession imaging using phase detection. *Magn Reson Med* 2003;50:210–213.
12. Reeder SB, Wen Z, Yu H, Pineda AR, Gold GE, Markl M, Pelc NJ. Multicoil Dixon chemical species separation with an iterative least squares estimation method. *Magn Reson Med* 2004;51:35–45.
13. Huang TY, Chung HW, Wang FN, Ko CW, Chen CY. Fat and water separation in balanced steady state free precession using the Dixon method. *Magn Reson Med* 2004;51:243–247.
14. Hargreaves BA, Nishimura DG. Quadratic fat/water separation in balanced SSFP. In: *Proceedings of the 13th Annual Meeting of ISMRM*, Miami Beach, FL, USA, 2005. p. 103.
15. Wieben O, Leupold J, Mansson S, Hennig J. Multi-echo balanced SSFP imaging for iterative Dixon reconstruction. In: *Proceedings of the 13th Annual Meeting of ISMRM*, Miami Beach, FL, USA, 2005. p. 2386.
16. Absil J, Denolin V, Metens T. Fat attenuation using a dual steady state balanced-SSFP sequence. In: *Proceedings of the 13th Annual Meeting of ISMRM*, Miami Beach, FL, USA, 2005. p. 104.
17. Leupold J, Scheffler K, Hennig J. Fast fat saturation for balanced SSFP imaging at low flip angles using alternating TR. In: *Proceedings of the 12th Annual Meeting of ISMRM*, Kyoto, Japan, 2004. p. 266.
18. Freeman R, Hill HDW. Phase and intensity anomalies in Fourier transform MRI. *J Magn Reson* 1971;4:366–383.
19. Sekihara K. Steady-state magnetizations in rapid NMR imaging using small flip angles and short repetition intervals. *IEEE Trans Med Imaging* 1987;MI6:157–164.
20. Nayak KS, Hu B, Hargreaves BA. Wideband SSFP: SSFP with imaging bandwidth greater than $1/TR$. In: *Proceedings of the 13th Annual Meeting of ISMRM*, Miami Beach, FL, USA, 2005. p. 2387.
21. Foxall DL. Frequency modulated steady state free precession imaging. *Magn Reson Med* 2002;48:502–508.
22. Deimling M, Heid O. Magnetization prepared true FISP imaging. In: *Proceedings of the 2nd Annual Meeting of SMR*, San Francisco, CA, USA, 1994. p. 495.
23. Speck O, Scheffler K, Hennig J. Fast 31P chemical shift imaging using SSFP Methods. *Magn Reson Med* 2002;48:633–639.
24. Deimling M, Heid O. TrueFISP imaging with inherent fat cancellation. In: *Proceedings of the 8th Annual Meeting of ISMRM*, Denver, CO, USA, 2000. p. 1500.